Cold expansion of rail-end-bolt holes: Finite element predictions and experimental validation by DIC and strain gauges

Giovanni Pio Pucillo [a]*, Alessandro Carrabs[a], Stefano Cuomo[b], Adam Elliott[c], Michele Meo[b]

[a]Department of Industrial Engineering, University of Naples Federico II, P. le V. Tecchio 80, 80125 Naples, Italy

[b]Department of Mechanical Engineering, University of Bath, Claverton Down, Bath BA2 7AY, UK

[c]Hird Rail Development Ltd, Clifford House, Lady Bank Drive, Lakeside, Doncaster DN4 5NF, UK

Keywords: Cold Expansion, Fatigue, Crack Growth, Strain Gauge, Digital Image Correlation, Finite Element Analysis

ABSTRACT

This paper provides experimental validation of a FE model simulating the cold-expansion of rail-end-bolt holes. Three rail holes were used for the experiments and, contrary to literature, hoop and radial strains were measured along different radial paths during the entire process using both electrical strain gauges and 2D-Digital Image Correlation. Residual and maximum strains predicted with the FE model agree well with measurements obtained with both experimental techniques, providing good confidence in the use of the proposed model to predict the effective stresses acting around the holes and to develop a LEFM-based model for crack growth simulation at cold-expanded holes.

1. Introduction

The improvement in terms of fatigue strength of structural parts is one of the most important topic of study in the academic and industrial world. Fatigue performance dependency on material properties [1] is well established and is dramatically influenced by stress concentrations, e.g. fastener holes, where fatigue cracks generally initiate [2–5].

In railways, fatigue is of particular interest, due to restrictive structural requirements for both rolling stock and track components. Cracks due to fatigue at rail holes of rail joints is a crucial issue in the railway superstructure [6,7], leading to early rails substitution, speed reductions and serious impacts on inspections and maintenance costs [8].

Rail joints are used to join the ends of adjoining rails and are divided in non-insulated or insulated [9]. While non-insulated rail joints are adopted for provisional repairs [10], insulated rail joints (IRJs) are designed to ensure transportation safety [11], to electrically isolate sections of track for signalling purposes [12] and to detect broken rails [13]. However, IRJs are prone to harsh duty loads [14] that can cause fatigue cracking at the hole surface [15]. This is due to high wheel/track impact forces [10,16] amplified by possible poorly compacted ballast [17,18], and reduced flexural stiffness than conventional rails. Moreover, because at the rail-end-bolt holes the cross section of the rail abruptly changes, a stress raiser is introduced, which increases the effect of loading conditions.

Because total stresses are given by the sum of residual stresses and those induced by external loads, fatigue life of metal parts can be increased by artificially induced compressive residual stresses in the most critical areas. Among the various common and cost-effective techniques, pad coining, ball expansion, direct mandrel expansion, split-sleeve cold expansion, and interference-fit fasteners, are applied in the aeronautical field to induce beneficial compressive residual stresses in the proximity of the border of holes, to increase the fatigue resistance of bolted and riveted structures [19]. In particular, split-sleeve cold expansion process was first proposed by Boeing in 1960s, and then developed by Fatigue Technology Incorporated [20], mainly for applications on aluminium alloys made aircraft components. However, thanks to the flexibility of the process, the split-sleeve cold expansion has been extended also to rail joints [8,21], and the RailTec System was specifically designed for the rail industry [22,23], see Fig. 1. Using this technique, an ill-fitting tapered mandrel, inserted in a graphite inner- treated split-sleeve, is pulled through the hole, causing yielding due to the radial expansion of an annular area encompassing the bore; when the process is completed, the surrounding material deformed elastically exerts compression onto the yielded annular area because tries to return to its original state (undeformed). The final effect is a compressive hoop stress distribution around the hole boundaries. The lubricated split sleeve has multiple benefits: reduction of pulling force, hole wall protection from deleterious frictional forces, surface roughness reduction, and trimming of irregularities due to machining operations [24].

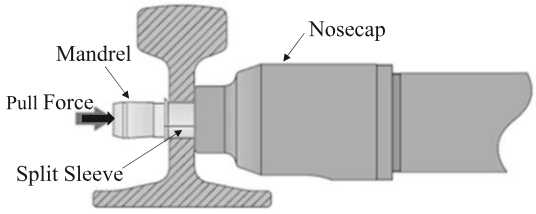

Fig. 1. Schematic diagram of the FTI RailTec System split-sleeve cold working setup.

Even though the fatigue resistance improvement obtained with cold expansion (CE) is widely recognized, a common procedure to establish the optimum degree of CE is lacking. Often, CE degree selection is based on the results of fatigue test campaigns executed with two or multiple levels of CE [24–26]. If the damage tolerant approach is used [27–33] and a predictive crack growth model is applied to set up inspections intervals [6,34–36], the CE degree selection process mentioned above is not fully satisfactory. Indeed, damage tolerant approach needs the actual stresses are known, in order to evaluate the stress intensity factor [2,4,5]. The latter, in turn, requires the a priori calculation of the residual stresses induced by CE. For this purpose, many approaches have been adopted, including experimental techniques, analytical models, and numerical simulations.

Common experimental methods adopted to evaluate residual stress field are: X-ray diffraction technique [26,37–45], neutron diffraction technique [45,46], the modified Sachs method [47], and the Garcia- Sachs method [48,49]. Unfortunately, all the mentioned techniques show some drawbacks: the X-ray diffractometer measures stresses only in the outer surface layers of the component [42] and moreover the output is affected by not acceptable accuracy in areas with high stress gradients; neutron diffraction technique is very complex and not easy to implement; the Sachs method is based on approximate formulations. Furthermore, the CE process is mostly applied in aerospace, hence most of the results of previous investigations referred mainly on drilled aluminium alloys parts or assemblies submitted or not to CE [26,37,50–54,38–40,42–45,48], representing mock-ups of real aeronautical components with riveted or bolted joints. Only few research works experimentally investigated CE on steel components [41,55], but none of them considered railway parts or structures, and in particular rail-end-bolt holes discussed in this paper.

In literature, various analytical models can be found for the evaluation of the residual stress field due to CE. Hsu and Forman [56] proposed an exact elastic-plastic solution for the residual stresses in a loaded infinite sheet, supposing an elastic unloading phase to simulate the mandrel extraction from the hole. Afterwards, other authors were able to consider the reverse yielding mechanism induced during the unloading phase for the plane strain case [57], and the influence of finite size of the plate under plane stress hypothesis [58]. However, analytical solutions rely on 2-D formulations and, for this reason, are not effective to predict both the variation through the thickness of residual stresses and the influence of complex geometries on the residual stress field.

Numerical – mainly finite element (FE) – approaches proposed in literature to simulate the CE process are generally divided in two types: uniform expansion models and contact analysis models. The first one simulates the hole expansion by applying radial displacements to the nodes belonging to the hole wall during the first step, whereas the spring-back mechanism of the material due to mandrel removal is obtained during the second step suppressing the previously imposed radial displacements. This approach is applied in 2-D plane stress/strain problems (not capable to estimate the through-thickness variation of the residual stresses), 2-D axisymmetric models (limited to simple geometries), and 3-D models [40,59–62]. The other approach involves contact simulation between the hole wall and the tapered mandrel, employing both 2-D axisymmetric and 3-D models [24,61–64]. In this case, axial displacement is applied to the mandrel model to generate the interference with the hole, which implies the progressive expansion of the latter and progressive spring-back of the material surrounding the hole during mandrel extraction. It is important to highlight that, despite uniform expansion models are unable to evaluate the nonsymmetric distribution of the residual stresses with respect the mid-thickness of the plate, they are fine for a first understanding of the residual stress field in the proximity of the holes. Finite element models simulating the contact between the mandrel and the surface of the hole, instead, provide more accurate results, but at the same time they are much more expensive in terms of time and computation resources. Also in this case, few FE researches have been proposed in literature to evaluate the residual stress field surrounding rail-end-bolt holes submitted to CE.

The novelty in this research work relies on the application of two experimental techniques, never used in literature, to investigate and determine the induced strain field during and after CE of rail-end-bolt holes. Successively, data from the experimental campaign are exploited for the validation of a FE model proposed in this study, simulating the CE process.

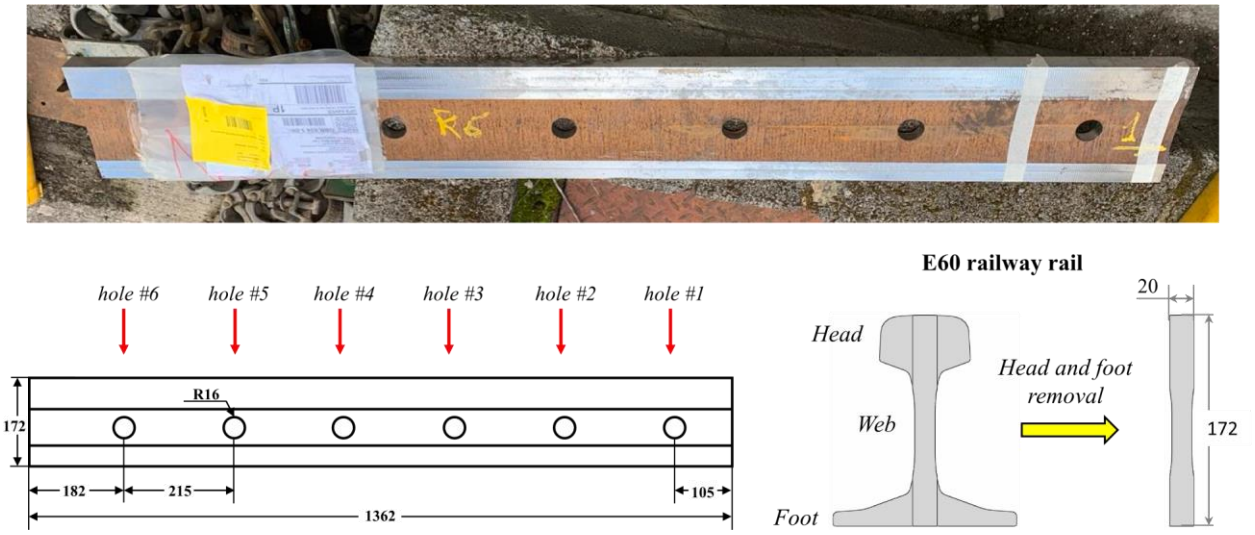

Fig. 2. Machined rail used for the experimental campaign.

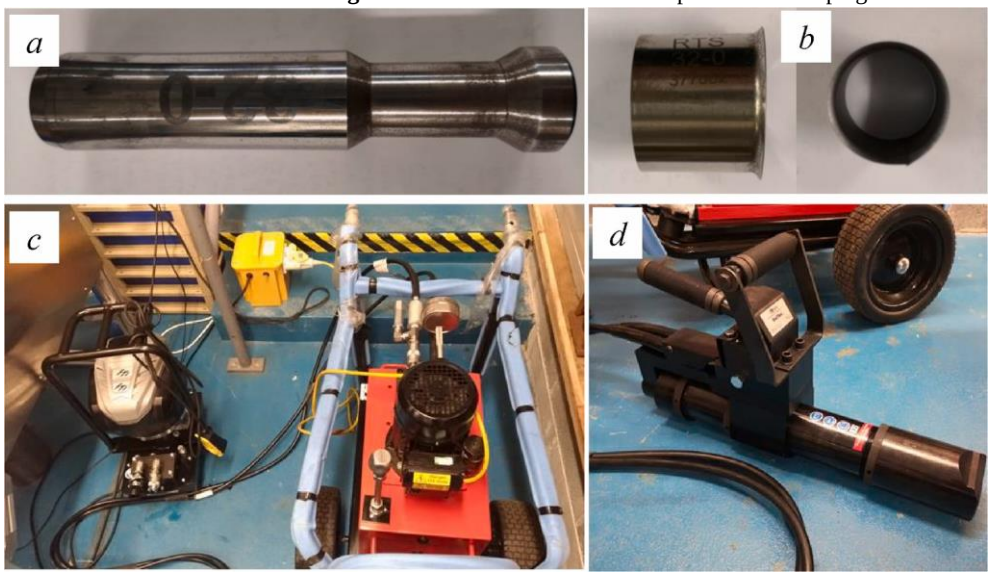

Fig. 3. FTI's equipment: tapered mandrel (a); self-lubricated split-sleeve (b); power units (c); pulling unit (d).

Data acquisition from the test campaign was performed with foil strain gauges (SGs) and two-dimensional Digital Image Correlation (2D- DIC). Furthermore, to exactly reproduce the real scenario and to check the repeatability of the results, CE was executed on three rail holes having same diameter used in IRJs, namely 32 mm.

Experimental research works on CE performed with SGs have been proposed in literature [53], but none of them focused on rail steels. Moreover, in this study SGs have been used to detect radial and hoop strain-time histories along different radial paths, including the ones where fatigue cracks usually propagate in not-expanded rail-end-bolt holes of IRJs, with the aim to appreciate the sensible non-linear elastic- plastic response of the material throughout the CE process and to acquire a wide range of results to validate the FE model proposed herein.

One of the most attractive features of the DIC relies in its capability to measure both displacements and strains in full-field conditions [65,66].

Moire photography ´ [67], Moire interferometry [68], and the grid method [26] are other full-field experimental methods adopted in the past to investigate CE; however, their main drawback compared to DIC is the considerable strains magnitude, that causes damages or distortions of the grids, with related difficult extraction of the fringe pattern. DIC technique was already applied to study the CE mechanism, but most of the research works considered drilled aluminium plates [69,70]. In this study, instead, 2D-DIC has allowed full-field evaluation of residual strains due to CE in the proximity of rail bolt holes.

The aim of the test campaign presented herein was to determine the repeatability of: the measurements; the cold expansion technique; the applied experimental procedures; and last but not least to deduce the radial and hoop strains distribution and their dependency on the distance from the hole border. Finally, a comparison between SGs and 2D- DIC data was executed to obtain a reliable non-linear result hint to be exploited during the FE model validation.

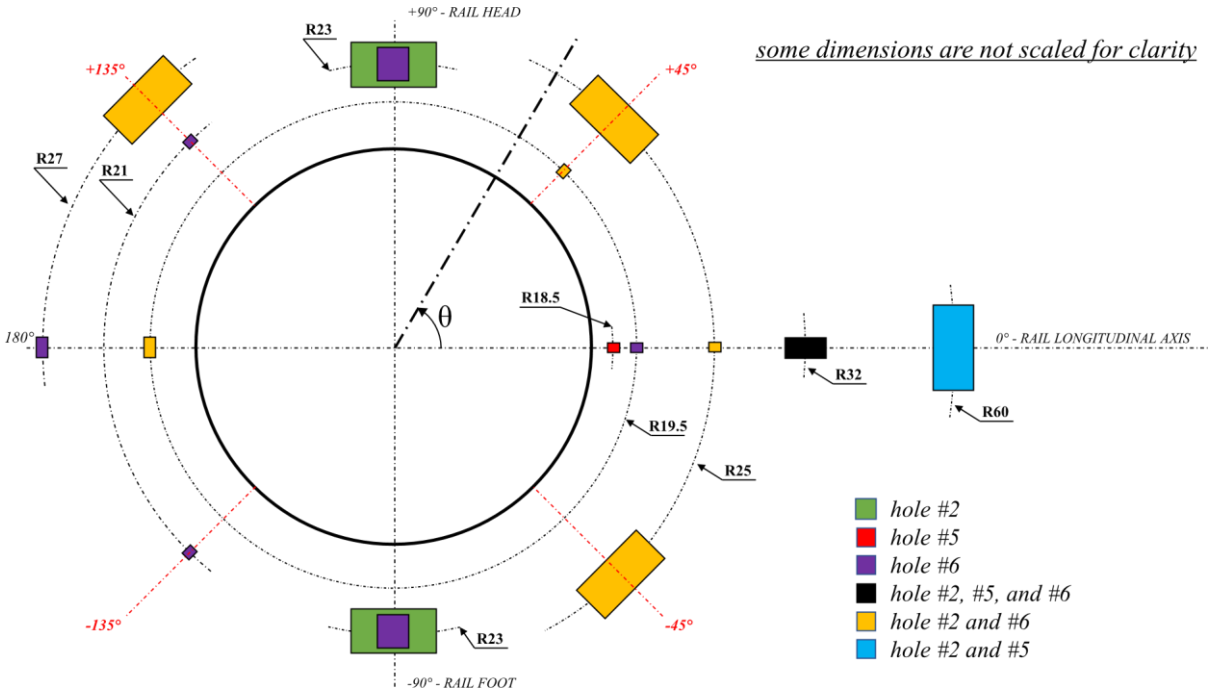

Fig. 4. Strain gauges locations for all the three holes to expand.

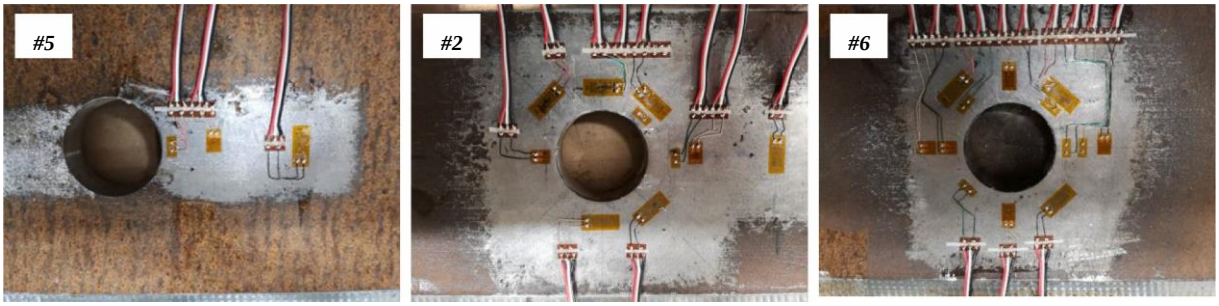

Fig. 5. Strain gauges applied near the three holes of the rail

The FE model presented in this study was realized on the assumption of uniform expansion approach. Afterwards, the strains acquired experimentally were used to validate the FE model. The 3D character of the stress field due to CE will be analysed, and its dependency on the degree of CE will be highlighted.

2. Experimental campaign

For the evaluation of the strain-time histories near rail-end-bolt holes during the split-sleeve CE process, a 60E1 rail segment with six holes having nominal diameter equal to that used in IRJs (32 mm) was considered. Before the execution of cold expansion, part of the foot and of the head have been machined (see Fig. 2), in order to generate the grip surfaces of the samples that will be fatigue tested, and that will be derived from CE and not CE drilled rails. In [71], FE simulations have demonstrated that the residual stress-strain fields induced by CE in the modified and original rail are almost equal, so the machined rail of Fig. 2 was considered representative of the actual rail.

Holes #5, #2, and #6 (see Fig. 2) were expanded by 2% using an FTI RTS 32-0 tapered mandrel, and a 0.3 mm thick RTS32-0 graphite inner- treated split-sleeve (see Fig. 3).

2.1. Specimen preparation

2.1.1. Strain gauges

For the measure of radial (ε_r) and hoop (ε_θ or ε_{hoop}) strain-time histories during CE, twenty-six electrical SGs were glued in proximity of holes #2, #5 and #6. SGs were applied on the rail web surface corresponding to the entry side of the mandrel, because the exit side is in contact with the pulling unit's nosepiece jaws during the CE process (see Fig. 1). The positions of the SGs are shown in Fig. 4 in cylindrical coordinates cantered on the hole, where the angular coordinate θ is the angle formed by the radial direction and the longitudinal axis of the rail. Finally, in Fig. 5 pics of the holes after bonding of the strain gauges are shown.

To gather meaningful data from the test campaign used then to validate the finite element model, strain gauges were applied in positions that guaranteed to appreciate the hoop and radial strains dependency on both the distance from the border of the hole and the angular coordinate θ. At the same time, special attention was paid for the evaluation of the strains distribution along specific directions of interest. In particular:

- the directions at $\theta = \pm 45^\circ$ are fundamental, being those along which crack paths are typically observed both in insulated and non- insulated rail joints [6,7,15];
- considering that future fatigue tests will be executed on expanded and not expanded specimens derived by drilled rails, and that the longitudinal axis of the rail identifies the minimum transversal section of the specimens, strain gauges were also mounted at $\theta = 0^\circ$;
- the strain field is expected to be not axisymmetric, hence some holes were instrumented with SGs positioned at the same distance from the border of the hole and at different angular coordinates; for example, as shown in Fig. 4, thanks to this setup was feasible to make a comparison between the hoop strains measured at $+90^\circ$ and -90° (hole #2), as well as the hoop strains acquired at $+45^\circ$ and -45° (hole #6).

Fig. 6. Speckle pattern (left) and strain gauges (right) on hole #2.

Finally, some strain gauges were applied in the same position on different holes, in order to verify whether both the experimental measurements and the CE process are repeatable. It is noteworthy to bear in mind that, because the strain gauge matrix width would have limited the spatial resolution of the measurements, symmetry condition with respect to the plane perpendicular to the rail axis and passing through the centre of the hole was employed. In this way, strain measurements made along symmetric radial paths – with respect to the trace plane $\theta = +90^\circ$ – were considered as if they were performed on the same radial path. In Fig. 4 (holes #2 and #6), SGs at $\theta = +135^\circ$ were glued far away from the border of the hole (at 11 mm, corresponding to R = 27 mm) than SGs at $\theta = +45^\circ$ (at 9 mm, corresponding to R = 25 mm), and all them were referred to the location $\theta = +45^\circ$ during the processing phase of the experiment (see Fig. 14-c).

2.1.2. Digital Image Correlation

A random speckle pattern on the side of the rail web where the mandrel enters through the hole was made using a base layer of white paint and then applying black matte paints. This was necessary because the rail had no textured surface to be detectable by the system. A sanding process was executed in order to ensure adhesion of the white base layer on the rail and avoid cracking of the paint layer during the CE process. The applied speckle patterns were specifically dimensioned to include all the SGs attached near the three holes. Calibration was executed using a known length from the field of view. Fig. 6 shows one of the three holes (hole #2), one half with the speckle pattern, the other one with the applied strain gauges.

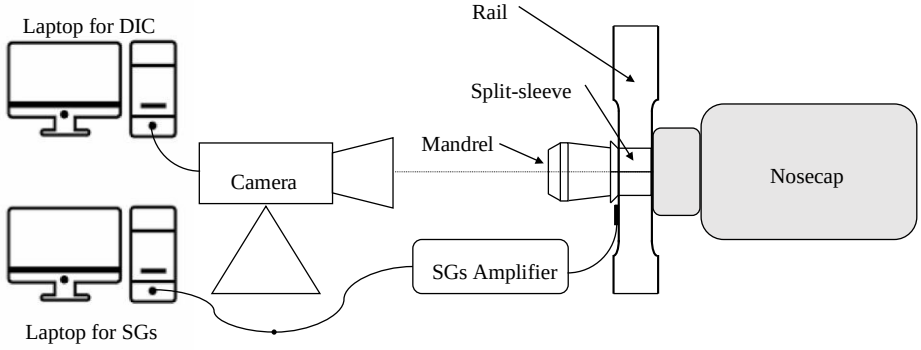

Fig. 7. Experimental setup diagram.

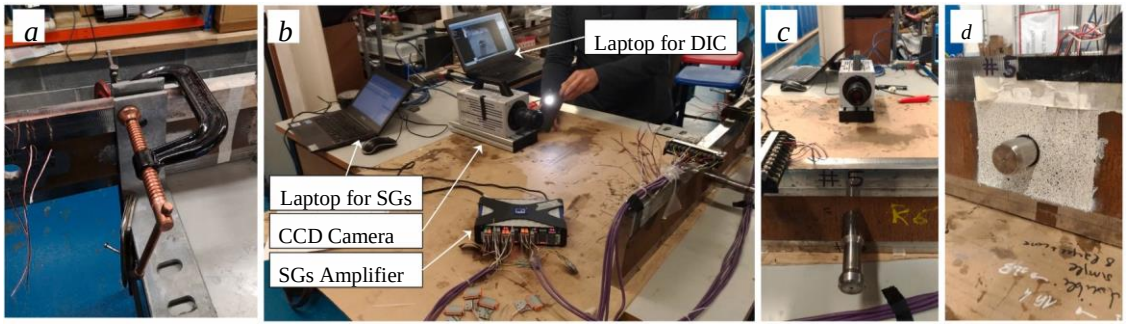

Fig. 8. (a) Fixing apparatus; (b) strain gauges and DIC setup; (c) mandrel exit side; (d) mandrel entry side.

2.2. Experimental setup

The diagram of the experimental setup is reported in Fig. 7, whereas Fig. 8 shows some photos taken in the laboratory. The specimen was fixed with three clamps and two L brackets made of steel (Fig. 8-a) to prevent unacceptable movements during the CE execution. The specimen was positioned upside, i.e. the rail foot (machined) facing downward and head (machined) facing upward.

To visualize, analyse, and store the strain-time histories measured by SGs during CE of the three holes, an HBM QuantumX MX1615B amplifier connected to a PC was employed (Fig. 8-b), setting a sampling rate of 50 Hz and using quarter-bridge 3-wire configuration for all the SGs. Catman AP software was chosen for real-time view and post-processing of strain gauge signals throughout the experimental campaign.

The DIC system consisted of a CCD camera, Photron Fastcam SA3 with Nikon AF Nikkor 50 mm f/1.8D lens connected via Ethernet to a high-performance PC (Fig. 8-b). The camera sensor was positioned specifically parallel to the inspected surface (Fig. 8-c). Settings management, shooting options, camera control and data storage were performed with Photron Fastcam Viewer (PFV) software. Spatial resolution of 1024 × 1024 pixels, recording time of 21.5 s (long enough to shoot the whole CE process) and 125 fps as frame rate were selected. As for strain gauges, for each hole to expand the images were captured on the entry side of the mandrel (Fig. 8-d), due to contact between the exit side and the puller nosepiece.

3. Finite element modelling

To calculate the stress-strain field due to different degrees of cold- expansion, a 3-D FE model was developed in Abaqus, version 6.11 [72], assuming isotropic behaviour of the material constituting the rail segment used for the experiments, specifically R260 steel. The engineering (or nominal) curve of the material, $\sigma_{eng} - \varepsilon_{eng}$, was determined averaging the experimental results of five uniaxial tensile tests, from which the Young's modulus, yield strength, and Poisson's ratio were found to be 210 GPa, 507 MPa, and 0.33, respectively. In Abaqus, the hardening behaviour of the material must be entered in tabular form, in terms of true stress, σ_{true}, vs. logarithmic plastic strain, ε^{p}_{ln}; therefore, using the relationship below:

$$\sigma_{true} = \sigma_{eng}\left(1 + \varepsilon_{eng}\right)$$

$$\varepsilon_{ln} = \ln\left(1 + \varepsilon_{eng}\right)$$

$$\varepsilon^{p}_{ln} = \varepsilon_{ln} - \frac{\sigma_{true}}{E}$$

E the $\sigma_{true} - \varepsilon^{p}_{ln}$ curve was deduced (Fig. 9-a) from the engineering curve, and then discretized in nine points (Fig. 9-b), as requested by Abaqus.

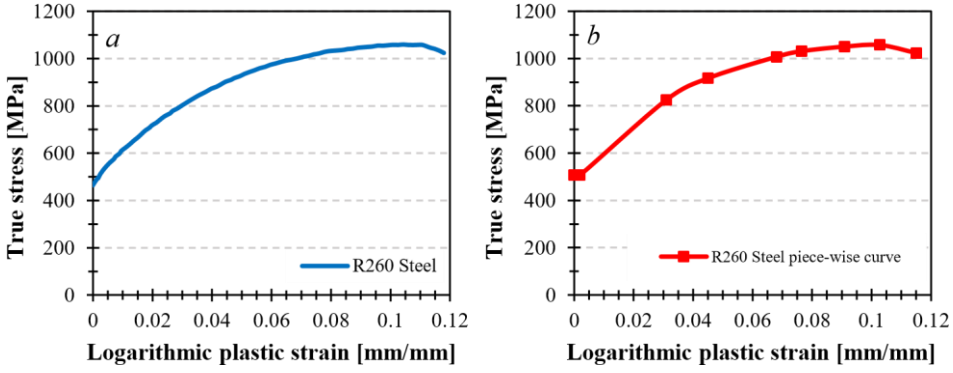

Fig. 9. Hardening curve of the R260 rail steel

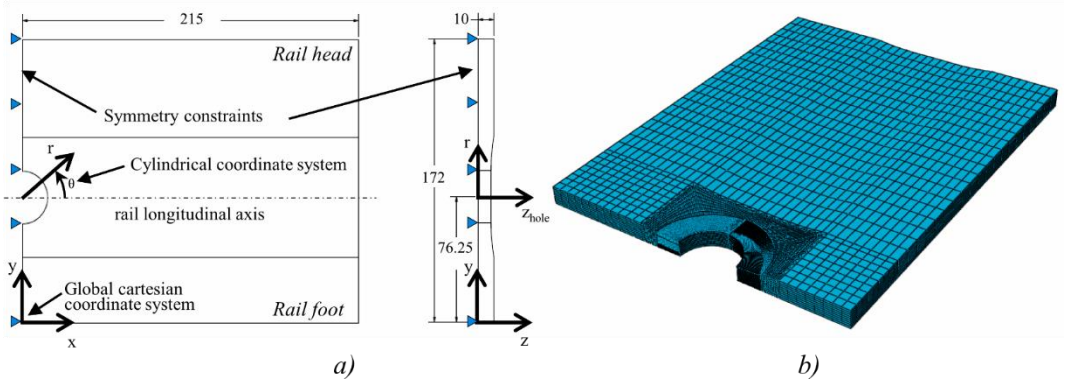

Fig. 10. FE model: dimensions and boundary constraints (a), and mesh (b

The 3-D FE model proposed in this study has been realized following the approach of uniform expansion models (see Section 1). Hence, on the nodes lying onto the hole surface, a uniform radial displacement was applied and then suppressed to simulate, respectively, the maximum hole/mandrel interference and the spring-back of the material due to mandrel extraction. Being the hole radius equal to 16.0 mm, radial displacements equal to 0.16 mm, 0.32 mm, and 0.64 mm were applied to simulate CE degrees equal to 1%, 2%, and 4%, respectively.

Consistent with the performed experimental investigations, the basic geometry is the one obtained cutting part of the head and of the foot from the 60E1 railway rail (see Fig. 2). In detail, a drilled machined rail 430 mm in length was considered and, as reported in Fig. 10, the quarter-symmetry model was used due to the double symmetry (transversal and longitudinal planes of the rail) in terms of geometry and boundary conditions. To take into account the remaining part of the geometry, to all the nodes lying on the planes XY and YZ of Fig. 10-a symmetry boundary conditions in Z and X directions, respectively, were applied.

The mesh of the FE model, Fig. 10-b, is made by 2619 6-node linear triangular prism elements and 85,698 8-node linear brick reduced integration elements, for a total of 98,600 nodes. A preliminary convergence analysis confirmed the adequacy of the element size used for the FEM simulations presented in this paper.

4. Results

4.1. Experimental results

In this Subsection, strain-time histories from SGs and residual strain distribution from 2D-DIC are shown. Equal degree of CE was expected for each hole, taking in consideration the rigorous tolerances in railways.
Hence, to verify the repeatability of measures; CE process; and the used experimental methods, at first data from SGs applied on each hole are synthesized, and a comparison between the measures on different holes is made. Afterwards, all the SGs data will be grouped as if only a single CE process was executed on a single hole; this allows the evaluation of hoop and radial strains dependency on both the distance from the border of the hole and the angular coordinate θ. Finally, 2D-DIC results are presented.

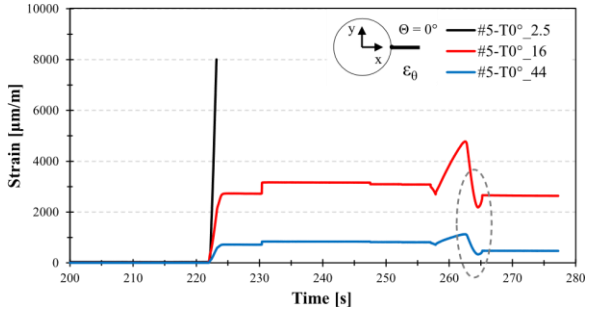

Fig. 11. Hole #5: hoop strain-time histories acquired by SGs.

4.1.1. Strain gauges

SGs signals measured in the course of the entire CE process executed on holes #5, #2, and #6 are reported, respectively, in Figs. 11–13, where common features can be noted, which are typical of the CE process. As mentioned previously, strain-time histories obtained during cold-expansion have never been presented in literature, at the time of writing. In the above figures, each strain gauge is identified by mean of the following nomenclature:

#N − Dθ_dfh,

with N the hole numbering, D identifies the strain component measured by the SG (D = "T" or "R" for hoop – or tangential – or radial strain, respectively), θ is the angular coordinate of the SG in the cylindrical coordinate system of Fig. 10-a (see also Fig. 4), and dfh is the distance of the SG from the border of the hole.

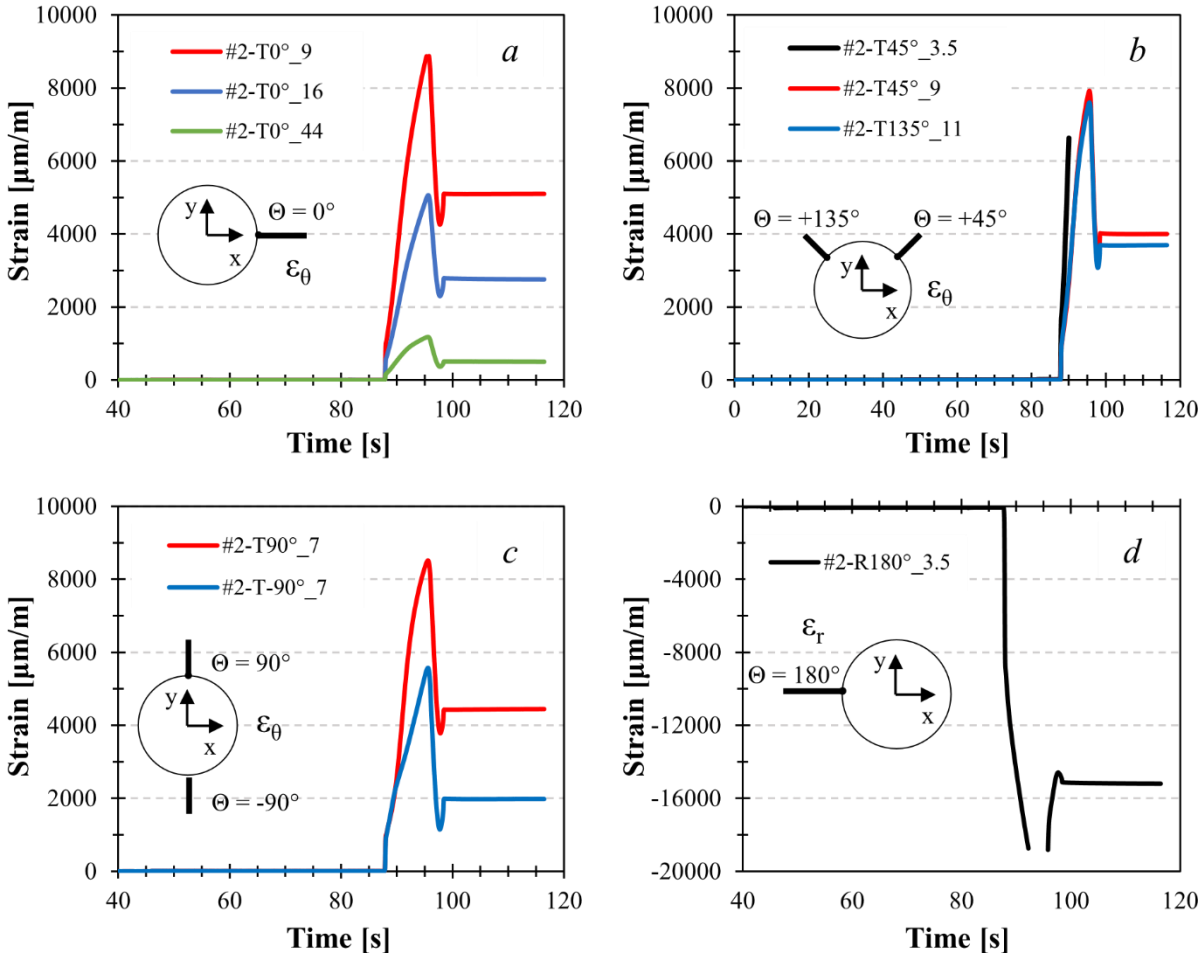

Fig. 12. Hole #2: hoop (a, b, c) and radial (d) strain-time histories acquired by SGs.

Throughout the CE process, hoop strains, ε_θ, are positive, whereas radial strains, ε_r, are negative. For each expanded hole, the measured hoop (radial) strains reached a maximum (minimum) value when the maximum hole/mandrel interference was achieved in the outer layers of the rail web surface corresponding to the mandrel entry side, where the SGs were applied. Successively, after mandrel removal, the hoop (radial) strains reached a local minimum (maximum) and then increased (decreased) up to the final values, representing the residual strains due to CE. As expected, both the maximum intensity and the residual value of strain acquired by each SG decrease moving away from the border of the hole.

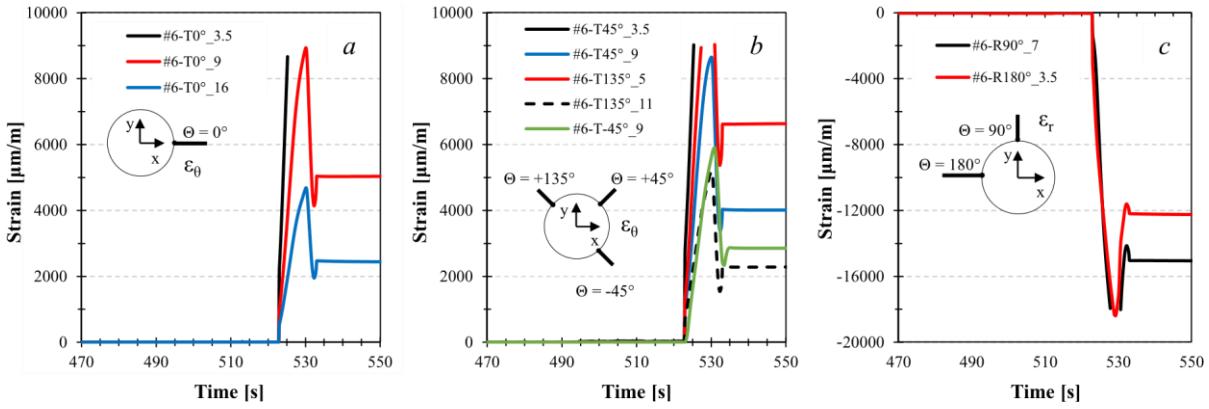

Fig. 13. Hole #6: hoop (a, b) and radial (c) strain-time histories acquired by SGs.

Both the local maximum (for radial strains) and local minimum (for hoop strains) acquired before the strains reached the residual values correspond to the cessation of the mandrel pulling action. Indeed, in the first phase of the mandrel/hole interaction, the conical part of the mandrel presses on the hole edge, producing bending of the rail web; as a consequence, on the instrumented surface of the rail web, corresponding to the mandrel entry side, positive radial strains (or radial strains increase) and, because of Poisson's effect, compressive hoop strains (or hoop strains decrease) are induced by bending of the rail web. In contrast, at the end of the CE process the mandrel/hole interaction terminates, so rail web bending vanishes and, consequently, hoop strains increase (see dotted ellipse in Fig. 11) and radial strains decrease on the rail web surface instrumented with SGs.

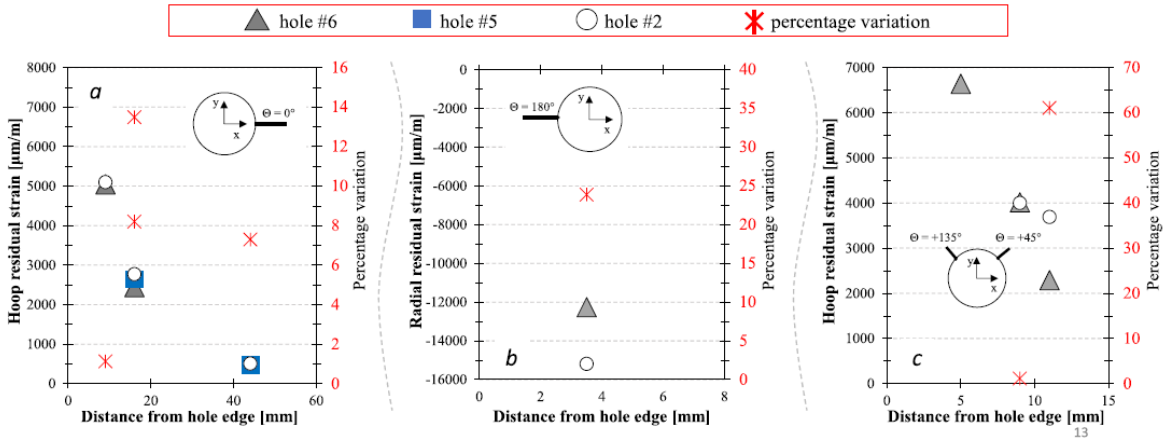

Fig. 14. Residual strains due to 2.0% of CE as a function of the distance from the hole edge and for different radial paths. On the secondary (right) vertical axes, percentage variation between SGs data acquired at the same position but on different holes.

Looking at the hoop strain-time histories acquired by the SGs installed at 2.5 mm (#5-T0◦_2.5, Fig. 11) and 3.5 mm (#2-T45◦_3.5, Fig. 12-b, #6-T0◦_3.5, Fig. 13-a, and #6-T45◦_3.5, Fig. 13-b) from the hole edge, it is possible to note that they interrupted during the CE process, presumably due to the high strain levels arising at short distances from the hole edge. Consequently, no signal processing was performed for them. In other cases, instead, while the maximum expansion of the hole was executed the signals have exceeded the valid range of the amplifier (#2-R180◦_3.5, Fig. 12-d; #6-T135◦_5, Fig. 13-b; #6-R90◦_7, Fig. 13-c), therefore for them the acquisition of the maximum intensity was not possible, instead during mandrel removal the signals reappeared in the valid amplifier range, so that the residual strains have been considered as correct. Fig. 14 synthesizes both the hoop and radial residual strains distribution along specific radial paths, using the experimental values acquired by groups of SGs having equal coordinates but glued in proximity of different holes (see Fig. 4). As expected, in all the graphs of Fig. 14 it can be noted that residual strains decrease in function of the distance from the edge of the hole. Moreover, in order to quickly check the repeatability of both the adopted experimental technique and the CE process, the secondary vertical axis of each graph reports the percentage differences between the residual strains measured by SGs having equal coordinates but referred to different holes. In detail, for each set of strains measured by SGs glued in the same location, the differences (in percentual terms) have been evaluated with

respect to the value of the lowest strain belonging to the above set; an exception is made for a single SG (Fig. 14-c, SG at 5 mm from the hole edge), being available only one SG applied on that position.

Hoop residual strains measured at $\theta = 0^\circ$ are reported in Fig. 14-a. Considering that equal degree of CE was expected for each hole (see Section 4.1), the strains are very similar, with a maximum difference between the measurements of about 13.5%. Radial residual strains concerning the path with $\theta = 180^\circ$ are reported in Fig. 14-b, where the difference between the measurements is around 23%. Thanks to symmetry with respect to the vertical diameter, it was assumed that the paths at $\theta = +45^\circ$ and $\theta = +135^\circ$ were sources of information referring to the same path, as aforementioned in Section 2.1.1, hence the distribution of the residual hoop strain was evaluated merging the signals of SGs applied along the mentioned directions ($+45^\circ$ and $+135^\circ$), as shown in Fig. 14-c. In this case, at a distance of 9 mm from the border of the hole strains are very similar (1% difference); a bigger difference (60%) was observed at 11 mm from the hole edge.

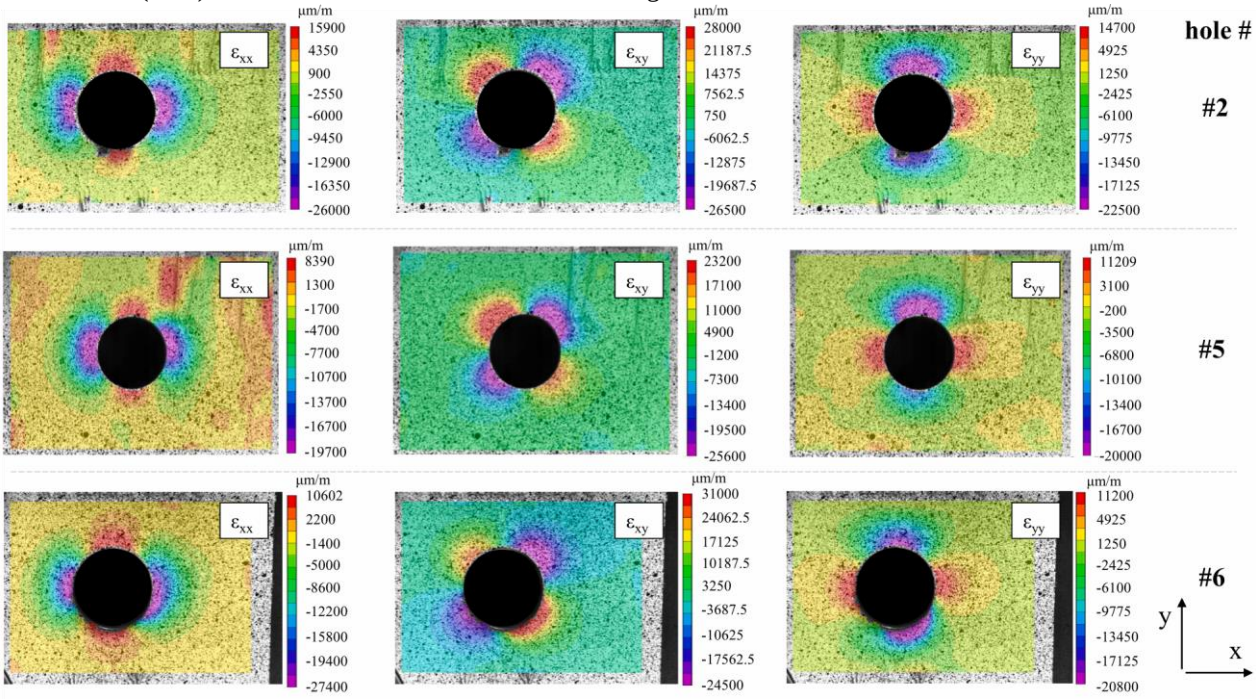

Fig. 15. 2D-DIC results: residual strains due to 2.0% of CE near the three holes of the rail web.

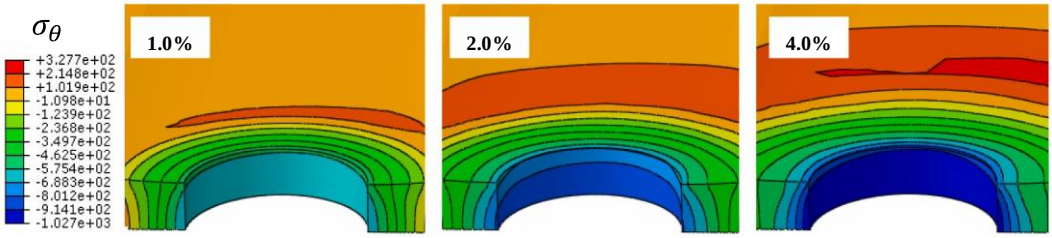

Fig. 16. Hoop residual stress distribution due to CE = 1%, 2%, 4%.

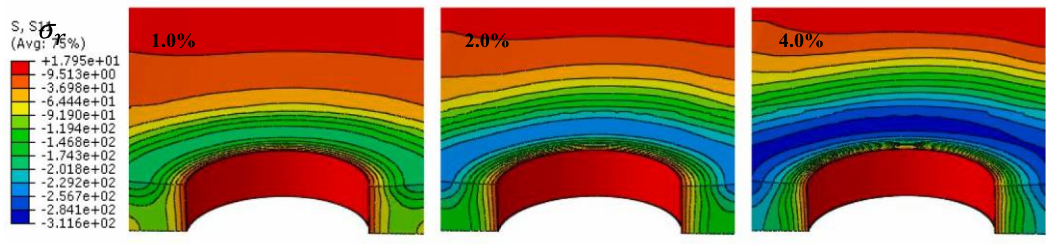

Fig. 17. Radial residual stress distribution due to CE = 1%, 2%, 4%.

In any case, apart from the last circumstance, consistency in the residual strains trend is appreciated, with a satisfying repeatability of the experimental results, giving good confidence of the collected data set, strictly related for the FE model validation.

4.1.2. Two-Dimensional DIC

Image post-processing was executed with Vic-2D software. As reference image, the one captured prior the mandrel has been put into the hole was selected. Correlation process was performed among the reference image and that captured when the mandrel was removed.

Normal residual strains (εxx and εyy) and shear residual strains (εxy) contour plots evaluated in the proximity of the CE holes are shown in Fig. 15, using the global cartesian coordinate system of Fig. 10 (see also the bottom right of Fig. 15). The images were post-processed with 17 px2 as subset size, 5 px as step size, and 15 as value for the strain filter window, for holes #2 and #6. To post-process hole #5, the same strain filter window was used, setting 43 px2 as subset size and 7 px as step size. The step size (overlap ratio) controls the spatial resolution, the subset size defines the area of the image used to track the displacement between images. Once defined the area of interest, and then choosing the subset and step size, the strain window dimension (computation size) is generated by Vic-2D software.

4.2. Finite element

In the first part of this subsection, residual stresses predicted by the FE model for different degrees of CE (1%, 2% and 4%) are presented and discussed, since they represent the expected beneficial effect for improving the fatigue strength of rail-end-bolt holes. At the end, both the residual strain field and the one corresponding to the phase of maximum hole expansion are shown in the case of CE degree equal to that used for the experiments, i.e. 2%, in view of the comparison between FE predictions and experimental data that will be discussed at the end of this study. Both stresses and strains calculated with the FE model are expressed in the cylindrical coordinate system of Fig. 10-a.

Figs. 16 and 17 show, respectively, the hoop and radial residual stress distributions due to the aforementioned degrees of CE; both figures clearly highlight the three-dimensional feature of the residual stress field, demonstrating that neither plane stress nor plane strain models are correct representations of the material response to cold expansion.

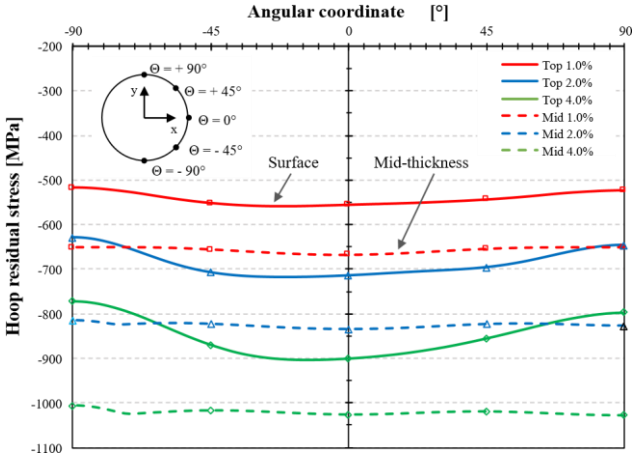

Fig. 18. Hoop residual stress distribution along the border of the hole (*Top*) and rail web mid-thickness (*Mid*) due to CE = 1%, 2%, 4%.

Both hoop (Fig. 16) and radial (Fig. 17) residual stresses vary along the thickness direction, and for any degree of CE the highest (compressive) residual hoop stress value is attained on the hole wall, at the rail web mid-thickness, whereas on the surface of the rail web highest (compressive) residual radial stresses are attained. Consistently with equilibrium condition, residual radial stresses after mandrel removal (Fig. 17) are approximately

zero (numerical zero) on the surface of the hole. From the same figures it can be noted that, as expected, the intensity of residual stresses decreases as the CE degree decreases: passing from 4% to 1%, the highest hoop stress reduces from 1027 MPa to 667 MPa, as well as the highest radial stress reduces from 312 MPa to 194 MPa.

Fig. 18 reports the distribution of the hoop residual stresses on the hole surface, specifically along the border of the hole ("Top") as well as on the rail web mid-thickness ("Mid"), allowing the gathering of more in-depth insight into the main effect of the CE process, i.e. the compressive tangential stresses, that is expected to guarantee fatigue life increase of rail-end-bolt holes. In detail, hoop residual stresses are reported as a function of the angle θ (see Fig. 10-a) and for different degrees of CE. From this figure it is possible to observe that on the hole border the predicted residual stress field varies with θ, in good agreement with literature.

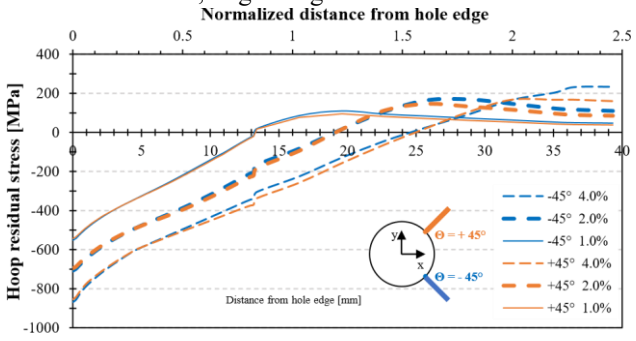

Fig. 19. Hoop residual stress distribution on the paths at $\theta = \pm 45^{\circ}$ due to CE = 1%, 2%, 4%.

In fact, as stated in [26,73], the efficacy of CE is affected by the gap between the edge of specimen and the edge of hole, having higher residual stress intensities with great distance values. Looking at the values of hoop residual stresses predicted on the surface of rail web at θ = +90◦, 0◦, − 90◦ (Fig. 18), it is worth noting that the lowest value is attained at θ = − 90◦, due to the smaller edge distance

(60.25 mm) than those at θ = +90◦ (79.75 mm) and at θ = 0◦ (199 mm), see Fig. 10-a. This result also agrees, in terms of residual strains, with the experimental measurements reported, e.g., in Fig. 12-c (strain gauges #2-T90◦_7 and #2-T-90◦_7), where it is found that $\varepsilon_{hoop,\,res}(\pi/2) > \varepsilon_{hoop,\,res}(-\pi/2)$. Conversely, hoop residual stresses are quite uniform at mid- thickness.

The empirical evidence shows that at not expanded rail-end bolt holes cracks generally initiate from the hole edge, i.e. on the rail web surface, and propagate along planes at ±45◦ with respect to the rail longitudinal axis [6,7,15], due to the action of pure shear stresses. Because from Fig. 18 it is possible to recognize that, as seen also in Fig. 16, for any degree of CE the intensity of residual stresses on the border of the hole are lower than those attained on the rail web mid- thickness, it seems correct to identify the rail web surface as the most likely site for fatigue crack initiation in CE holes as well, and ±45◦ as the expected direction along which fatigue crack paths will develop.

Therefore, the prediction of hoop residual stresses at θ = ±45◦, i.e. the residual stresses perpendicular to the – expected – crack surface, is crucial to evaluate the corresponding mode I stress intensity factor due to residual stresses, KI-res, aiming to establish a linear elastic fracture mechanic (LEFM) model for the prediction of crack propagation [4,26,27,74].

For this purpose, Fig. 19 shows, for different degrees of CE, the hoop residual stresses predicted on the surface of the rail web for θ = ±45◦. On the hole edge, the hoop residual stress reaches the highest compressive magnitude, while moving away from the border it changes from compression to tension, reaches the highest tensile value, then progressively decays to zero. When the CE degree is reduced from 4% to 1%:

- the highest compressive hoop stress decreases from 854 MPa to 543 MPa along $\theta = +45^{\circ}$, and from 869 MPa to 551 MPa along $\theta = -45^{\circ}$;
- the highest tensile hoop stress varies from 167 MPa to 95 MPa at $\theta = +45^{\circ}$, and from 233 to 109 MPa along $\theta = -45^{\circ}$;
- the extension of the zone submitted to residual compression reduces from about 1.55 to about 0.83 times the radius of the hole, both along $\theta = +45^{\circ}$ and $\theta = -45^{\circ}$.

Finally, as shown in Fig. 20, both maximum and residual strains due to 2% of cold expansion were evaluated as a function of the distance from the hole edge, in order to achieve the indispensable dataset for the FE model

validation discussed successively. Maximum intensities of hoop and radial strains were calculated for θ = 0◦, ±45◦, and ±90◦ when the maximum hole/mandrel interference is realized (Fig. 20-a), i.e. at the end of the first step of the FE analysis (see Sections 1 and 3). Same measures were executed in terms of residual strains (Fig. 20-b), i.e. at the end of the second step of the FE simulation.

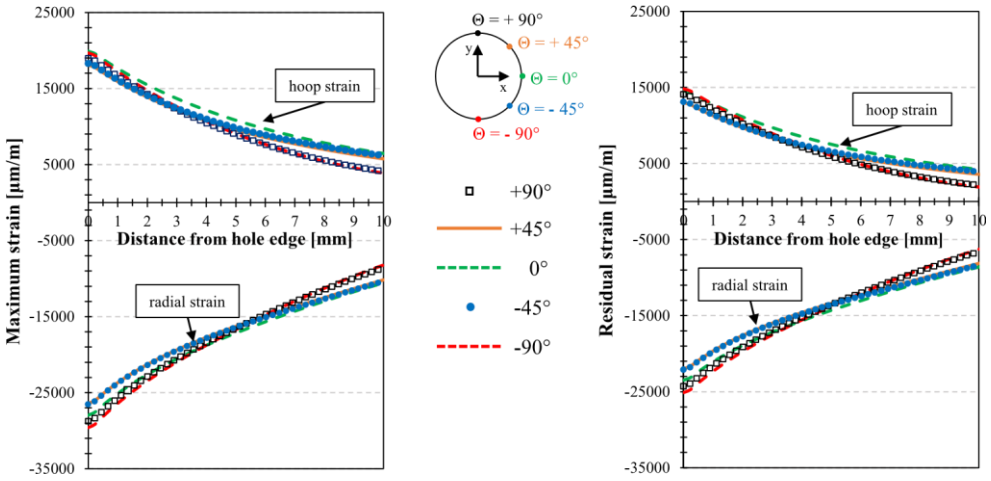

Fig. 20. Maximum (a) and residual (b) strain distribution on the paths at $\theta = 0^{\circ}$, $\theta = \pm 45^{\circ}$, and $\theta = \pm 90^{\circ}$ due to CE = 2%.

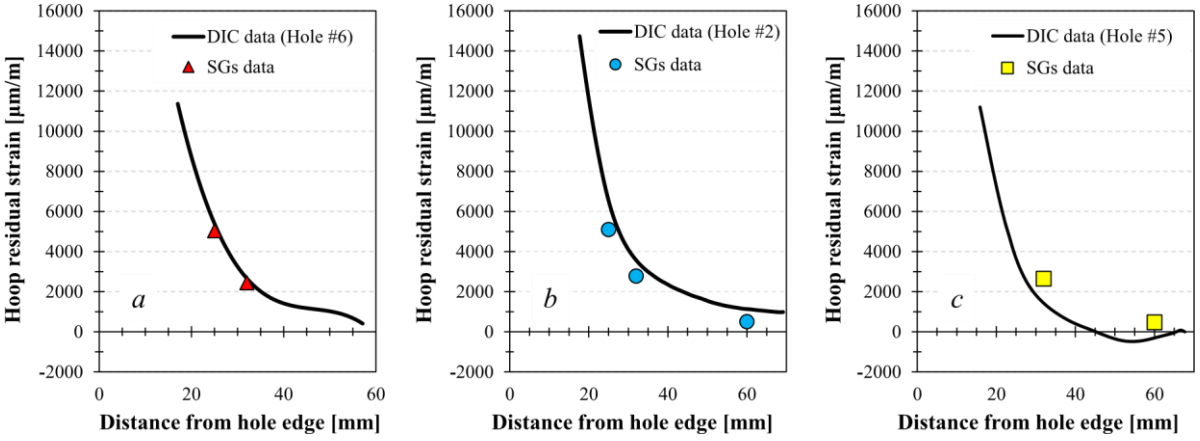

Fig. 21. Hoop residual strains after 2.0% of CE on each hole: 2D-DIC vs. SGs data.

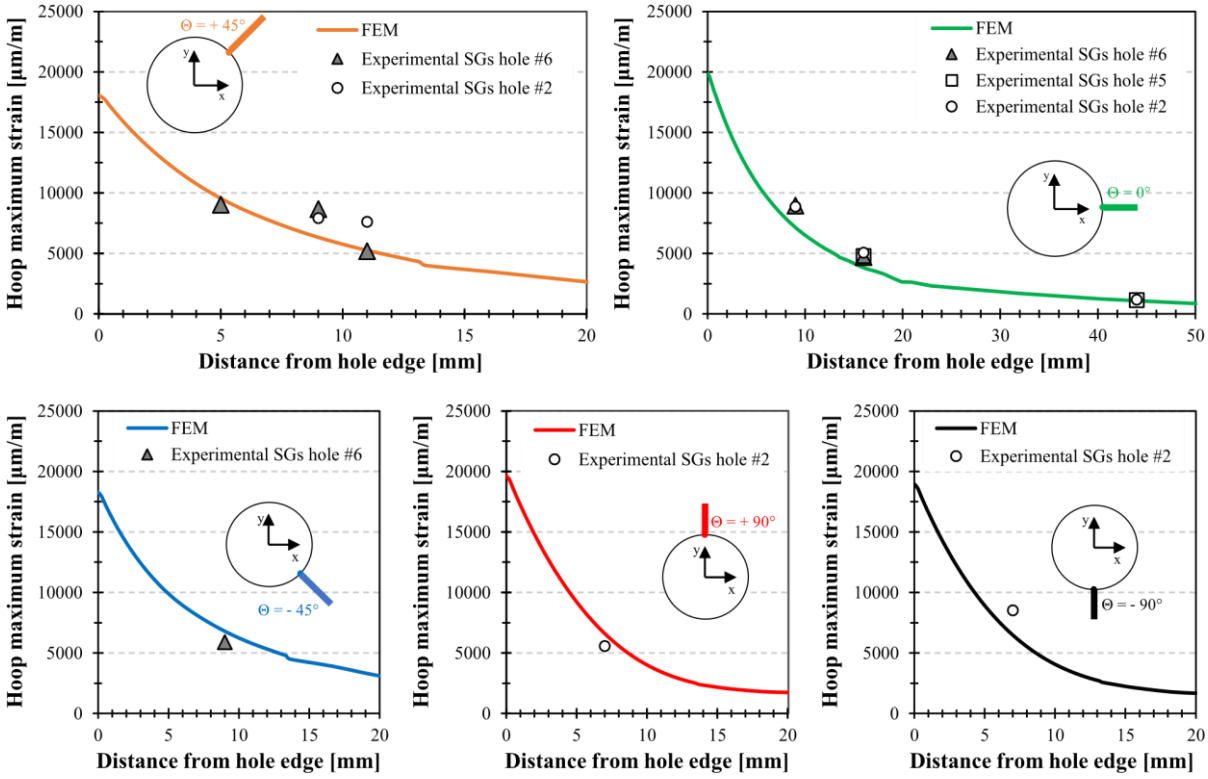

Fig. 22. Hoop maximum strains for 2.0% of CE: FE predictions vs. SGs data along the directions at 0°, ±45°, and ±90

5. Discussion

5.1. Strain gauge vs. Two-Dimensional DIC data

Hereafter the comparison between experimental data from SGs and 2D-DIC is reported. Only for the flat portion of the rail web surface the residual strains acquired with 2D-DIC are assumed to be consistent, since the 2D method is restricted to in-plane strains and displacements of a surface without warpage. Because the flat portion of the rail web corresponds exactly to a rectangle 32 mm high and containing the generatrixes of the hole intercepted by the angles $\theta = -90^{\circ}$ and $\theta = 90^{\circ}$ (Fig. 2), comparison is limited to data from the SGs located at $\theta = 0^{\circ}$, i.e. on the longitudinal axis of the rail.

In Fig. 21, hoop residual strains measured on holes #2, #5 and #6 after 2% of CE are reported, where it is found that image correlation results track perfectly the SGs measurements for hole #6 (Fig. 21-a), with a difference around 5%. The residual strains trend detected by 2D- DIC agrees with SGs measurements for hole #2 as well (Fig. 21-b), but higher difference (around 25%) than hole #6 is observed though. This could be addressed to unwanted rigid motions of the rail during the CE or to poor speckle pattern quality. Indeed, even though the rail was clamped (see Section 2.2), considering the energy required to pull the mandrel through the hole, small out-of-plane displacements could be occurred during the expansion process. SGs and image correlation data are not quite consistent for hole #5 (Fig. 21-c). This disagreement of the data is plausibly caused by the considerations discussed for hole #2 (poor speckle pattern and rail movements), indeed a non-perfect alignment of the camera with the rail was noted at the end of the expansion process, badly affecting the results.

5.2. Experimental data vs. Finite element predictions

In this subsection, maximum and residual strains predicted with the FE model are compared with those acquired with the experiments. Such comparison has never been discussed in literature, at the time of writing, and furthermore is fundamental for the FE model reliability. In elastic- plastic analyses, indeed, the comparison of the

current state of the material, i.e. the experimental points, with FE predictions in correspondence of several instants of the loading history is crucial [75], being the whole stress-strain field the result of a path-dependent phenomenon. In the case of CE, the instants mentioned above are represented by the phase of maximum hole expansion and by the phase of mandrel removal.

In Fig. 22, hoop maximum strains acquired by SGs along the directions at θ = 0◦, ±45◦, and ±90◦ are compared with those predicted with the FE model, where a good agreement is appreciated.

In Fig. 23, instead, SGs measurements and FE predictions of hoop residual strains concerning the paths at θ = ±45◦ and ±90◦ are compared. Along the directions θ = +45◦ and θ = − 90◦ the results are consistent, whereas some disagreements are observed at $\theta = -45^{\circ}$ and $\theta = +90^{\circ}$.

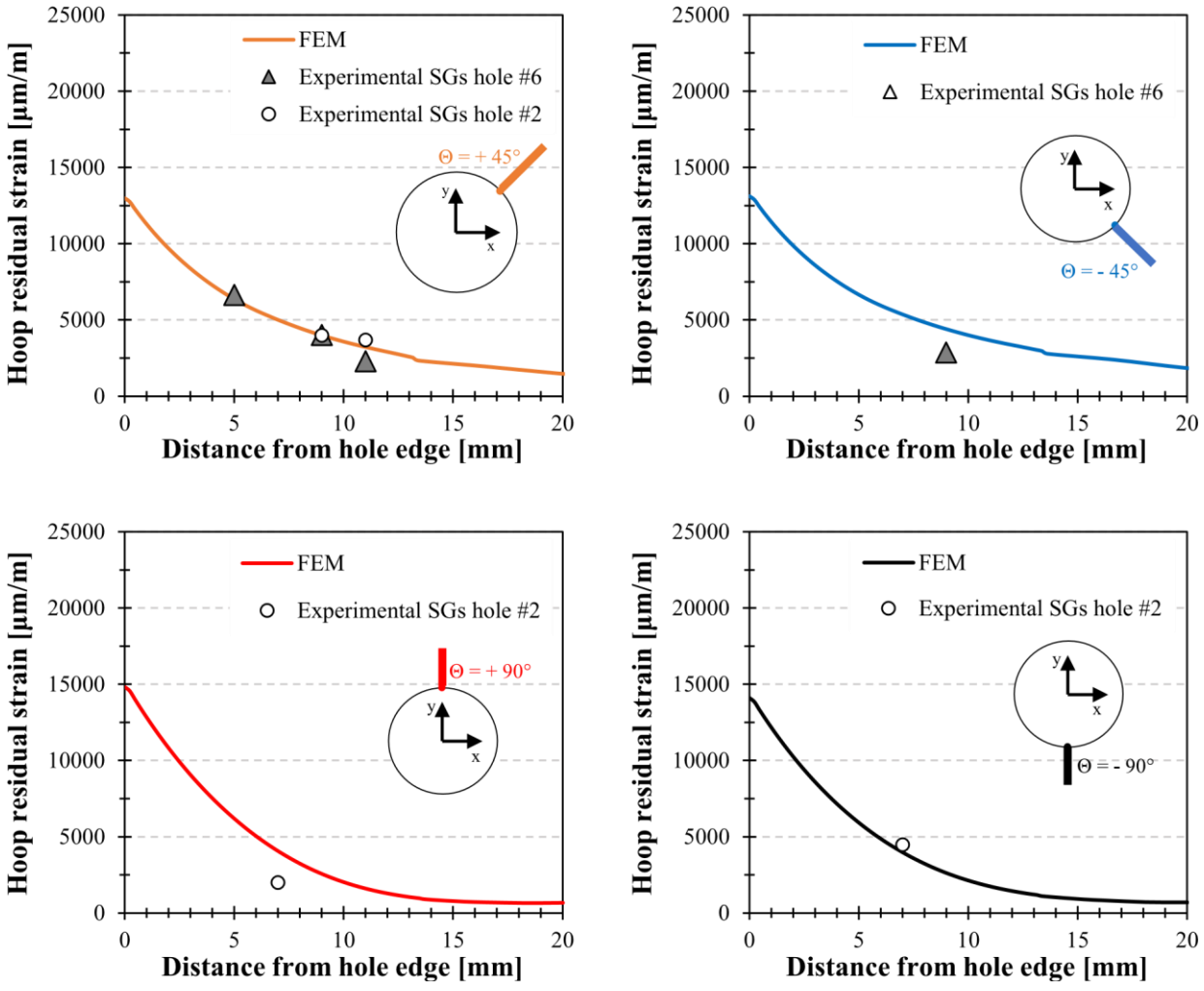

Fig. 23. Hoop residual strains for 2.0% of CE: FE predictions vs. SGs data along the directions at ±45° and ±90°

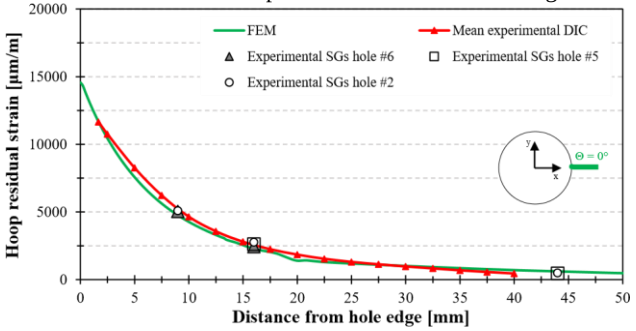

Fig. 24. Hoop residual strains for 2.0% of CE: FE predictions vs. SGs vs. DIC data along the direction at 0°.

Fig. 24, instead, shows the comparison of the hoop residual strains along the only path in which, in addition to the SGs data and FE predictions, the measurements obtained with 2D-Digital Image Correlation are also available, i.e. θ = 0◦: an excellent agreement is observed between the FEM results, the strain gauges data, and the average ("Mean Experimental DIC" curve) of the hoop residual strains measured by 2D- DIC on each hole. In detail, the values of the "Mean Experimental DIC" curve, ε_θ mean, were calculated as follow:

$$\varepsilon_\theta^{mean}(d) = \frac{\left[\varepsilon_\theta^{\#2}(d) + \varepsilon_\theta^{\#5}(d) + \varepsilon_\theta^{\#6}(d)\right]}{3}$$

where d =(dfh) represents the radial distance from the edge of the hole, and $\varepsilon^{\#i}{}_\theta(d)$ is the hoop residual strain measured by 2D-DIC for hole #i (i = 2, 5, 6).

Finally, in Fig. 25 the maximum and residual values of the radial strains calculated with the FE model are compared with those measured with SGs along θ = +90◦, whereas for θ = 0◦ only radial residual strains are considered. Also, for the radial strains, a good correlation is observed between numerical predictions and experimental data.

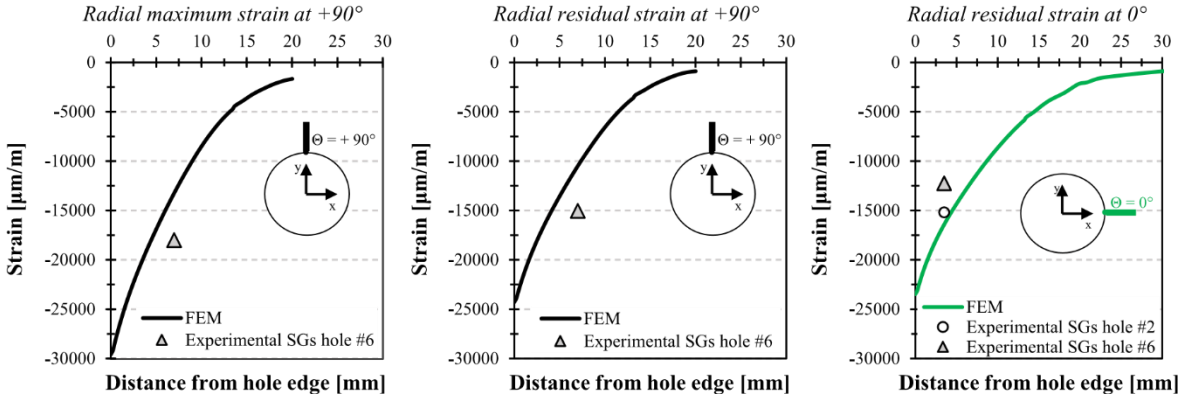

Fig. 25. Comparison of simulation results and measurement results of radial maximum strains along the direction at +90° and of residual strains along directions at +90° and 0°.

Briefly condensing the aforementioned discussion, FE estimations and experimental results are in good agreement, validating the FE model developed in this work. The FE model could be reliably adopted, then, for the prediction of the effective stress field arising in the proximity of CE holes, which is the main requisite for the realization of a predictive crack growth model to be used in the framework of a damage tolerant approach for the design and maintenance of insulated and non-insulated rail joints.

6. Conclusions

The influence of CE on rail-end-bolt holes has been investigated through a three-dimensional FE model and an experimental campaign conducted under full-scale conditions on a real component.

Three rail holes have been submitted to cold expansion, applying two experimental methods: SGs and 2D-DIC. SGs have been used to measure

hoop and radial strain-time histories along different radial paths emanating from the hole edge, including those recognized as typical in fatigue fracture of insulated and non-insulated rail joints. Strain-time histories allowed to acquire precious experimental information during the loading history of the material surrounding the hole, in particular when the maximum hole expansion is achieved and at material recovery after mandrel removal, whereas the DIC method enabled full-field measure of the residual strains in the proximity of the edge of the hole. Such analyses have never been proposed and discussed in literature, and the good agreement between DIC and strain gauges results could be the kernel of a reliable and invaluable reference dataset (highly non-linear) on this topic, that in this study was exploited for the FE model validation.

The FE simulations clearly show the complex features of the residual stress field, being three-dimensional and not axisymmetric in the proximity of the rail hole. Residual stresses distribution and intensity are dependent on the CE degree, and moreover differences of residual stresses within the rail web thickness are considerable.

Remarkable consistency was noted between FEM predictions, strain gauges data, and DIC results, for the residual strain field estimation and during the phase of maximum hole expansion. This outcome provides good confidence in the use of the proposed FE model to estimate the actual stresses affecting CE rail-end-bolt holes, in order to create a predictive crack growth model to be used in the framework of a damage tolerant approach for the design and maintenance of these critical points of the railway superstructure.

Declaration of Competing Interest

The authors declare that they have no known competing financial interests or personal relationships that could have appeared to influence the work reported in this paper.

Acknowledgements

The authors greatly acknowledge RFI S.p.A, the Infrastructure Manager of the Italian State Railway, and Mr. Steve Coombes of the University of Bath, UK, for specimen instrumentation.

References

[1] Pucillo GP, Grasso M, Penta F, Pinto P. On the Mechanical Characterization of Materials by Arcan-Type Specimens. Eng Fract Mech 2011;78(8):1729–41.

[2] Carpinteri A. Handbook of Fatigue Crack Propagation in Metallic Structures - Volume 2. In: Carpinteri A, editors. Amsterdam: Elsevier; 1994. p. 834.

[3] Carpinteri A, Brighenti R, Vantadori S. Notched shells with surface cracks under complex loading. Int J Mech Sci 2006;48(6):638–49.

[4] Carpinteri A, Ronchei C, Vantadori S. Stress Intensity Factors and Fatigue Growth of Surface Cracks in Notched Shells and Round Bars: Two Decades of Research Work. Fatigue Fract Eng Mater Struct 2013;36(11):1164–77.

[5] Carpinteri A, Ronchei C, Scorza D, Vantadori S. Fracture mechanics based approach to fatigue analysis of welded joints. Eng Fail Anal 2015;49:67–78.

[6] Zerbst U, Lunden R, Edel K-O, Smith RA. Introduction to the Damage Tolerance´ Behaviour of Railway Rails – a Review. Eng Fract Mech 2009;76(17):2563–601.

[7] Cannon DF, Edel K-O, Grassie SL, Sawley K. Rail Defects: An Overview. Fatigue Fract Eng Mater Struct 2003;26(10):865–86.

[8] Reid L. Beneficial Residual Stresses at Bolt Holes by Cold Expansion. Rail Qual Maintenance Modern Railway Oper 1993:337–47.

[9] Carolan ME, Jeong DY, Perlman AB. Engineering Studies on Joint Bar Integrity, Part II: Finite Element Analyses. 2014 Joint Rail Conference, JRC 2014. Colorado Springs, CO, USA, paper #JRC2014-3708; 2014.

[10] Talamini B, Jeong DY, Gordon J. Estimation of the Fatigue Life of Railroad Joint Bars. ASME/IEEE 2007 Joint Rail Conference and Internal Combustion Engine Division Spring Technical Conference. Pueblo, Colorado, USA, paper #JRC/ ICE2007-40065; 2007.

[11] Esveld C. Modern Railway Track. 2nd ed. Delft, The Netherlands: MRT- Productions; 2001. p. 654.

[12] Himebaugh AK, Plaut RH, Dillard DA. Finite Element Analysis of Bonded Insulated Rail Joints. Int J Adhes Adhes 2008;28(3):142–50.

[13] Jeong DY, Bruzek R, Tajaddini A. Engineering Studies on Joint Bar Integrity, Part I: Field Surveys and Observed Failure Modes. 2014 Joint Rail Conference, JRC 2014.
Colorado Springs, CO, USA, paper #JRC2014-3706; 2014.

[14] Kerr AD, Cox JE. Analysis and Tests of Boned Insulted Rail Joints Subjected to Vertical Wheel Loads. Int J Mech Sci 1999;41(10):1253–72.

[15] Mayville RA, Stringfellow RG. Numerical Analysis of a Railroad Bolt Hole Fracture Problem. Theor Appl Fract Mech 1995;24(1):1–12.

[16] Mandal NK, Dhanasekar M, Sun YQ. Impact Forces at Dipped Rail Joints. Proc Inst Mech Eng, Part F: J Rail Rapid Transit 2016;230(1):271–82.
[17] De Iorio A, Pucillo GP, De Vita G, Musella S, Rossi S, Testa M, et al. The Reliability of the Locking Devices of the Switches. Role of the Ballast Bed. Int Rev Model Simul 2016;9(6):473–8.
[18] Pucillo GP, De Iorio A, Rossi S, Testa M. On the Effects of the USP on the Lateral Resistance of Ballasted Railway Tracks. 2018 ASME Joint Rail Conference, JRC 2018. Pittsburgh, Pennsylvania, USA, paper #JRC2018-6204; 2018.
[19] Fu Y, Ende G, Honghua S, Jiuhua X, Renzheng L. Cold Expansion Technology of Connection Holes in Aircraft Structures: A Review and Prospect. Chin J Aeronaut 2015;28(4):961–73.
[20] Restis J, Reid L. FTI Process Specification 8101D: Cold Expansion of Holes Using the Standard Split Sleeve System and Countersink Cold Expansion. Andover Park West, Seattle (WA), USA: Fatigue Technology Inc.; 2002.
[21] Cannon DF, Sinclair J, Sharpe KA. Improving the fatigue performance of bolt holes in railway rails by cold expansion. In: Goel VS, editor. Proceedings of the International Conference and Exposition on Fatigue, Corrosion Cracking, Fracture Mechanics and Failure Analysis. Salt Lake City, Utah: American Society for Metals (ASM); 1986. p. 353–69.
[22] Fatigue Technology Inc. RailTecTM System, FTI Process Specification 2009-03 Revision E; 2016.
[23] Fatigue Technology Inc.. FTI Process Specification 8101 Revision K; 2017.
[24] Chakherlou TN, Vogwell J. The Effect of Cold Expansion on Improving the Fatigue Life of Fastener Holes. Eng Fail Anal 2003;10(1):13–24.
[25] Chakherlou TN, Taghizadeh H, Aghdam AB. Experimental and Numerical Comparison of Cold Expansion and Interference Fit Methods in Improving Fatigue Life of Holed Plate in Double Shear Lap Joints. Aerosp Sci Technol 2013;29(1): 351–62.
[26] Ball DL, Lowry DR. Experimental Investigation on the Effects of Cold Expansion of Fastener Holes. Fatigue Fract Eng Mater Struct 1998;21(1):17–34.
[27] Carpinteri A. Shape Change of Surface Cracks in Round Bars under Cyclic Axial Loading. Int J Fatigue 1993;15(1):21–6.
[28] Carpinteri A, Brighenti R, Vantadori S. Notched double-curvature shells with cracks under pulsating internal pressure. Int J Press Vessels Pip 2009;86(7): 443–53.
[29] Carpinteri A, Vantadori S. Sickle-Shaped Surface Crack in a Notched Round Bar under Cyclic Tension and Bending. Fatigue Fract Eng Mater Struct 2009;32(3): 223–32.
[30] De Iorio A, Grasso M, Penta F, Pucillo GP. Fatigue Crack Growth Simulation in Railway Axles. Key Eng Mater 2012;488–489:407–10.
[31] De Iorio A, Grasso M, Kotsikos G, Penta F, Pucillo GP. Development of Predictive Models for Fatigue Crack Growth in Rails. Key Eng Mater 2012;488–489:13–6.
[32] Pucillo GP, Esposito L, Leonetti D. On the Effects of Unilateral Boundary Conditions on the Crack Growth Rate under Cycling Bending Loads. Int J Fatigue 2019;124: 245–52.
[33] Pucillo GP, Esposito L, Leonetti D. Boundary Conditions Effects on the Crack Growth Mechanism Under Cycling Bending. 2019 ASME Joint Rail Conference, JRC 2019. Snowbird, Utah, USA, paper #JRC2019-1274; 2019.
[34] Zerbst U, Schodel M, Heyder R. Damage Tolerance Investigations on Rails. Eng¨ Fract Mech 2009;76(17):2637–53.
[35] Zerbst U, Beretta S. Failure and Damage Tolerance Aspects of Railway Components. Eng Fail Anal 2011;18(2):534–42.
[36] De Iorio A, Grasso M, Penta F, Pucillo GP. A Three-Parameter Model for Fatigue Crack Growth Data Analysis. Frattura ed Integrita Strutturale 2012;21:2` 1–9.

[37] Pina JCP, Dias AM, de Matos PFP, Moreira PMGP, de Castro PMST. Residual Stress Analysis near a Cold Expanded Hole in a Textured Alclad Sheet Using X-Ray Diffraction. Exp Mech 2005;45(1):83–8.
[38] Shao XJ, Liu J, Liu YS, Yue ZF. Experiment and FEM Simulation on Residual Stress of Cold Expansion Hole. Mater Sci Forum 2007;561–565:1783–6.
[39] Shuai H, Youli Z, Zhihai C, Yanli W, Yongheng N, Xiaokun D. Effect of Hole Cold Expansion on Fatigue Performance of Corroded 7B04-T6 Aluminium Alloy. Int J Fatigue 2019;126:210–20.
[40] Priest M, Poussard CG, Pavier MJ, Smith DJ. An Assessment of Residual-Stress Measurements around Cold-Worked Holes. Exp Mech 1995;35(4):361–6.
[41] Zhao C, Hu H, Zhou Y, Gao Y, Ren X, Yang Q. Experimental and Numerical Investigation of Residual Stresses around Cold Extrusion Hole of Ultrahigh Strength Steel. Mater Des 2013;50:78–84.
[42] Cook R, Holdway P. Residual Stresses Induced by Hole Cold Expansion. Comput Methods Exp Measur Surface Treatment Effects 1993;2:91–100.
[43] de Matos PFP, Moreira PMGP, Pina JCP, Dias AM, de Castro PMST. Residual Stress Effect on Fatigue Striation Spacing in a Cold-Worked Rivet Hole. Theor Appl Fract Mech 2004;42(2):139–48.
[44] Stefanescu D, Edwards L, Fitzpatrick ME. X-Ray Diffraction Measurement of the Residual Stresses Surrounding a Cold Expanded Hole. Mater Sci Forum 2002; 404–407:185–90.
[45] Stefanescu D, Dutta M, Wang DQ, Edwards L, Fitzpatrick ME. The Effect of High Compressive Loading on Residual Stresses and Fatigue Crack Growth at Cold Expanded Holes. J Strain Anal Eng Design 2003;38(5):419–27.
[46] Luzin V, Gnaupel-Herold T, Gordon JE, Prask HJ. Neutron Residual Stress Measurements on Rail Sections for Different Production Conditions. IMECE2004, ASME International Mechanical Engineering Congress. Anaheim, California, USA, paper #IMECE2004-61754; 2004.
[47] Ozdemir AT, Edwards L. Measurement of the Three-Dimensional Residual Stress¨ Distribution around Split-Sleeve Cold-Expanded Holes. J Strain Anal Eng Design 1996;31(6):413–21.
[48] Garcia-Granada AA, Lacarac V, Smith DJ, Pavier MJ, Cook R, Holdway P. 3D Residual Stresses around Cold Expanded Holes in a New Creep Resistant Aluminium Alloy. Trans Eng Sci 1999;25:103–16.
[49] Garcia-Granada AA, Smith DJ, Pavier MJ. A New Procedure Based on Sachs' Boring for Measuring Non-Axisymmetric Residual Stresses. Int J Mech Sci 2000;42(6): 1027–47.
[50] Lacarac V, Smith DJ, Pavier MJ, Priest M. Fatigue Crack Growth from Plain and Cold Expanded Holes in Aluminum Alloys. Int J Fatigue 2000;22(3):189–203.
[51] Zuccarello B, Di Franco G. Numerical-Experimental Method for the Analysis of Residual Stresses in Cold-Expanded Holes. Exp Mech 2013;53(4):673–86.
[52] Amrouche A, Mesmacque G, Garcia S, Talha A. Cold Expansion Effect on the Initiation and the Propagation of the Fatigue Crack. Int J Fatigue 2003;25:949–54.
[53] Gopalakrishna HD, Narasimha Murthy HN, Krishna M, Vinod MS, Suresh AV. Cold Expansion of Holes and Resulting Fatigue Life Enhancement and Residual Stresses in Al 2024 T3 Alloy - An Experimental Study. Eng Fail Anal 2010;17(2):361–8.
[54] Ozelton M, Coyle T. Fatigue Life Improvement by Cold Working Fastener Holes in 7050 Aluminum. In: Potter J, editor. Fatigue in Mechanically Fastened Composite and Metallic Joints ASTM STP 927. Philadelphia, PA: ASTM; 1986. pp. 298.
[55] Lindh DV, Taylor RQ, Rose DM. Sleeve Expansion of Bolt Holes in Railroad Rail. US Federal Railroad Administration, Office of Research and Development; 1980.
[56] Hsu YC, Forman RG. Elastic-plastic analysis of an infinite sheet having a circular hole under pressure. J Appl Mech 1975;42(2):347–52.
[57] Rich DL, Impellizzeri LF. Fatigue Analysis of Cold-Worked and Interference Fit Fastener Holes. In: Impellizzeri LF, editor. Cyclic Stress-Strain and Plastic Deformation Aspects of Fatigue Crack Growth ASTM STP 637. West Conshohocken, PA: ASTM; 1977. p. 223.
[58] Wanlin G. Elastic-plastic analysis of a finite sheet with a cold-worked hole. Eng Fract Mech 1993;46(3):465–72.

[59] Kang J, Johnson WS, Clark DA. Three-dimensional finite element analysis of the cold expansion of fastener holes in two aluminum alloys. J Eng Mater Technol 2002;124(2):140–5.
[60] de Matos PFP, Moreira PMGP, Camanho PP, de Castro PMST. Numerical Simulation of Cold Working of Rivet Holes. Finite Elem Anal Des 2005;41(9–10): 989–1007.
[61] Yongshou L, Xiaojun S, Jun L, Zhufeng Y. Finite element method and experimental investigation on the residual stress fields and fatigue performance of cold expansion hole. Mater Des 2010;31(3):1208–15.
[62] Houghton SJ, Campbell SK. Identifying the residual stress field developed by hole cold expansion using finite element analysis. Fatigue Fract Eng Mater Struct 2012; 35(1):74–83.
[63] Maximov JT, Duncheva GV, Ganev N, Bakalova TN. The benefit from an adequate finite element simulation of the cold hole expansion process. Eng Fail Anal 2009;16 (1):503–11.
[64] Yasniy P, Glado S, Iasnii V. Lifetime of aircraft alloy plates with cold expanded holes. Int J Fatigue 2017;104:112–9.
[65] Pan B, Qian K, Xie H, Asundi A. Two-Dimensional Digital Image Correlation for in- Plane Displacement and Strain Measurement: Areview. Meas Sci Technol 2009;20 (6):062001.
[66] Pan B. Digital Image Correlation for Surface Deformation Measurement: Historical Developments, Recent Advances and Future Goals. Meas Sci Technol 2018;29(8): 082001.
[67] Cloud GL. Measurement of Strain Fields near Coldworked Holes. Exp Mech 1980; 20(1):9–16.
[68] Link RE, Sanford RJ. Residual Strains Surrounding Split-Sleeve Cold Expanded Holes in 7075–T651 Aluminum. J Aircraft 1990;27(7):599–604.
[69] Backman D, Liao M, Crichlow L, Yanishevsky M, Patterson EA. The Use of Digital Image Correlation in a Parametric Study on the Effect of Edge Distance and Thickness on Residual Strains after Hole Cold Expansion. J Strain Anal Eng Design 2008;43(8):781–9.
[70] Backman D, Cowal C, Patterson EA. Analysis of the Effects of Cold Expansion of Holes Using Thermoelasticity and Image Correlation. Fatigue Fract Eng Mater Struct 2010;33(12):859–70.
[71] Pucillo GP. Study and Modelling of the Cold Expansion Technique for Holes of the Railway Superstructure - Definition of the Reference Numerical Model and Determination of the Experimental Characteristic Curve [Studio e Modellizzazione della Tecnica di Espansione a Freddo per Fori nell'Armamento Ferroviario], REPORT LS-P0117, Department of Industrial Engineering, University of Naples Federico II, October 2019; 2019.
[72] Simulia DS. Abaqus 6.11 Theory Manual. RI, USA: Providence; 2011.
[73] Lowry DR. D6ac Steel Bolt Hole Life Improvement, F-111 Coldwork Modification Development Program (Phase II). Tech Rep 1991;FZS-12.
[74] Leonetti D, Maljaars J, Snijder HH. Fracture Mechanics Based Fatigue Life Prediction for a Weld Toe Crack under Constant and Variable Amplitude Random Block Loading - Modeling and Uncertainty Estimation. Eng Fract Mech 2021;242: 107487.
[75] Lee Y, Barkey ME. Fundamentals of Cyclic Plasticity Theories. In: Lee Y, Barkey ME, Kang H, editors. Metal Fatigue Analysis Handbook. Walthman MA, USA: Butterworth-Heinemann; 2012. p. 632.